Micropterons, nanopterons and solitary wave solutions to the diatomic Fermi–Pasta–Ulam–Tsingou problem

Faver , T.E.; Hupkes, H.J.

Micropterons, nanopterons and solitary wave solutions to the diatomic Fermi–Pasta–Ulam–Tsingou problem

Timothy E. Faver [a],[*], Hermen Jan Hupkes [b]

[a] *Department of Mathematics, Kennesaw State University, 850 Polytechnic Lane, MD #9085, Marietta, GA 30060, United States of America*
[b] *Mathematical Institute, Universiteit Leiden, P.O. Box 9512, 2300 RA Leiden, The Netherlands*

ABSTRACT

We use a specialized boundary-value problem solver for mixed-type functional differential equations to numerically examine the landscape of traveling wave solutions to the diatomic Fermi–Pasta–Ulam–Tsingou (FPUT) problem. By using a continuation approach, we are able to uncover the relationship between the branches of micropterons and nanopterons that have been rigorously constructed recently in various limiting regimes. We show that the associated surfaces are connected together in a nontrivial fashion and illustrate the key role that solitary waves play in the branch points. Finally, we numerically show that the diatomic solitary waves are stable under the full dynamics of the FPUT system.

1. Introduction

In this paper we study the Fermi–Pasta–Ulam–Tsingou (FPUT) equation[1],[2]

$$m_j \ddot{x}_j = F(x_{j+1} - x_j) - F(x_j - x_{j-1}), \qquad j \in \mathbb{Z} \qquad (1.1)$$

in the diatomic regime

$$m_j = \begin{cases} 1, & j \text{ is odd,} \\ m, & j \text{ is even,} \end{cases} \qquad (1.2)$$

using the quadratic spring force $F(r) = r + r^2$. In particular, we numerically investigate several branches of diatomic traveling waves that have recently been shown to exist for this system. Using a continuation approach, we track these branches outside of the parameter regimes where they have been rigorously constructed. This allows us to shed light on the intricate structure of the broader landscape of such solutions.

1.1. Propagation in discrete media

By now, the FPUT system (1.1) is well-established as a classic prototype of the propagation of disturbances through spatially discrete

systems, such as granular media, artificial metamaterials, DNA strands, and electrical transmission lines.[3],[4] In essence, it models an infinite, one-dimensional chain of particles that can only move horizontally and are connected to their nearest left and right neighbors by nonlinear springs. In the relative displacement coordinates

$$r_j = x_{j+1} - x_j, \qquad (1.3)$$

these springs transmit a force $F(r_j)$ between the particles at sites j and $j+1$. Applying Newton's law, this leads naturally to the evolution (1.1) for the position variables x_j; see Fig. 1. We do note that various other studies incorporate higher-order terms into the force $F(r)$,[5]–[7] but these can typically be handled using refined perturbative techniques[8] provided that the displacements from equilibria remain sufficiently small.

Traveling waves have played a fundamental role in the analysis of (1.1) and other spatially discrete systems.[4],[9]–[12] In the current diatomic setting, such solutions take the form

$$r_j(t) = \begin{cases} \overline{r}_o(j + \sigma t), & j \text{ is odd,} \\ \overline{r}_e(j + \sigma t), & j \text{ is even,} \end{cases} \qquad (1.4)$$

which means that the speed σ and the pair of wave profiles $(\overline{r}_o, \overline{r}_e)$ must satisfy the two-component mixed-type functional differential equation[1]
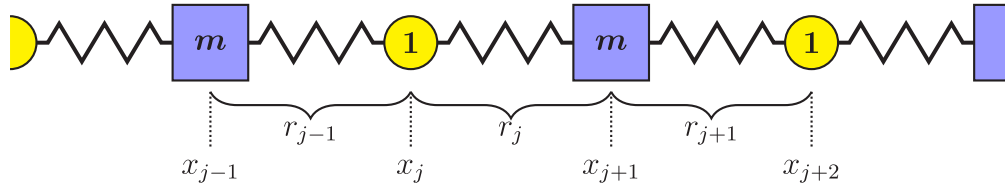

Fig. 1. The diatomic FPUT lattice, featuring alternating masses m and 1 connected by identical springs.

(MFDE)

$$\begin{cases} \sigma^2 \bar{r}_o''(\xi) = \frac{1}{m} F\big(\bar{r}_e(\xi+1)\big) - \Big(1 + \frac{1}{m}\Big) F\big(\bar{r}_o(\xi)\big) + F\big(\bar{r}_e(\xi-1)\big) \\ \sigma^2 \bar{r}_e''(\xi) = F\big(\bar{r}_o(\xi+1)\big) - \Big(1 + \frac{1}{m}\Big) F\big(\bar{r}_e(\xi)\big) + \frac{1}{m} F\big(\bar{r}_o(\xi-1)\big). \end{cases} \qquad (1.5)$$

The argument shifts in this system prevent the use of powerful ODE-techniques such as phase-plane analysis. This causes many technical complications in the analysis of spatially discrete systems; see, e.g., Ref. 13 for an overview of the machinery that has been developed for MFDEs.

1.2. Formal limits

The complexity of (1.5) can be reduced considerably by taking various (formal) limits. We briefly sketch three procedures of this type that play an important role in this paper.

1.2.1. Equal mass limit

Taking $m = 1$, the diatomic lattice becomes monatomic and one can set $\bar{r}_o = \bar{r}_e = \phi$ to arrive at the scalar MFDE

$$\sigma^2 \phi''(\xi) = F\big(\phi(\xi+1)\big) - 2F\big(\phi(\xi)\big) + F\big(\phi(\xi-1)\big). \qquad (1.6)$$

This is a classical problem that was analyzed in detail by Friesecke in combination with Wattis[14] and Pego,[5,15–17] who established that there exists a smooth branch of nontrivial solitary waves (σ, ϕ_σ) that are even, exponentially localized, and stable. In particular, for small $\epsilon > 0$ one can write

$$\sigma_\epsilon = 1 + \frac{\epsilon^2}{24}, \qquad (1.7)$$

and show that the associated profiles ϕ_{σ_ϵ} satisfy the limiting behavior[5]

$$\left\| \frac{8}{\epsilon^2} \phi_{\sigma_\epsilon}(2\epsilon^{-1}\cdot) - \mathrm{sech}^2(\cdot) \right\|_{H^1} = \mathcal{O}(\epsilon^2). \qquad (1.8)$$

More recently, Herrmann and Matthies[6,18,19] considered the "high-energy" limit $c \gg 1$, using a different Lennard-Jones-type potential for the springs that is analytic at $r = 0$ but singular at $r = 1$.

1.2.2. Small mass limit

Multiplying (1.5) by m and formally setting $m = 0$, the injectivity of F on $[0, \infty)$ yields the identification

$$\bar{r}_o(\xi) = \bar{r}_e(\xi+1). \qquad (1.9)$$

Physically, this means that the mass-less particles are fixed halfway between the heavier ones, corresponding with the intuition developed in Refs. 20, 21. Upon setting

$$\varphi(\xi) = \frac{1}{2}\bar{r}_o(2\xi) + \frac{1}{2}\bar{r}_e(2\xi+1) \qquad (1.10)$$

and adding the first line of (1.5) to a shifted version of the second line, the identification (1.9) readily reveals the MFDE

$$\sigma^2 \varphi''(\xi) = 2\big[F\big(\varphi(\xi+1)\big) - 2F\big(\varphi(\xi)\big) + F\big(\varphi(\xi-1)\big)\big]. \qquad (1.11)$$

If $\sigma \gtrsim \sqrt{2}$, then a solution to (1.11) is $\varphi := \phi_{\sigma/\sqrt{2}}$, where $\phi_{\sigma/\sqrt{2}}$ solves (1.6). That is, solitary waves can be expected for $\sigma \gtrsim \sqrt{2}$. The extra scaling corresponds to the notion that the effective limiting monatomic lattice has double the spring length of the original diatomic lattice. This is exactly how Hoffman and Wright[20] generate their limiting solitary waves.

1.2.3. Long wave limit

Here we fix $m \neq 1$ and make the classical long wave scaling[22]

$$\bar{r}_o(\xi) = \epsilon^2 \theta_o(\epsilon\xi; \epsilon) \qquad \text{and} \qquad \bar{r}_e(\xi) = \epsilon^2 \theta_e(\epsilon\xi; \epsilon). \qquad (1.12)$$

Upon making the further perturbation ansatz

$$\theta_o(X; \epsilon) = \sum_{k=0}^{3} \epsilon^k u_k(X) \qquad \text{and} \qquad \theta_e(X; \epsilon) = \sum_{k=0}^{3} \epsilon^k v_k(X), \qquad (1.13)$$

one can subsequently solve the traveling wave Eqs. (1.5) formally to $\mathcal{O}(\epsilon^4)$ by taking

$$u_1 = v_1 = \Phi_m, \qquad \sigma = \sigma_m^{(s)} + \mathcal{O}(\epsilon^2) \qquad (1.14)$$

and defining the other u_k and v_k in more complicated terms of the profile Φ_m. Here the speed of sound is

$$\sigma_m^{(s)} := \sqrt{\frac{2}{1+m}} \qquad (1.15)$$

and the solitary wave profile Φ_m satisfies the KdV traveling wave equation

$$a_m \Phi'' - \Phi + b_m \Phi^2 = 0, \qquad (1.16)$$

where a_m and b_m are (complicated) m-dependent coefficients, see Ref. 23, Eq. (3.2). That is,

$$\Phi_m(X) := \frac{3}{2b_m} \mathrm{sech}^2\left(\frac{X}{2\sqrt{a_m}}\right). \qquad (1.17)$$

We note that $\sigma_m^{(s)}$ reduces to the critical values found above for $m = 1$ and $m = 0$.

In a certain sense, this procedure can be seen as a specialization of the techniques developed in Ref. 24 and Ref. 25. Here the authors consider monatomic respectively polyatomic[2] FPUT systems and derive a set of KdV PDEs to approximate the evolution of suitably scaled initial conditions over algebraically long time-scales.

As we discussed at the start of Section 1.1, we are using the smooth spring force $F(r) = r + r^2$ throughout this paper. Allowing a nonsmooth force in the diatomic lattice introduces exciting complications and behaviors beyond the scope of our analysis. Nonetheless, one can sensibly pose a long wave limit for forces beyond our F; for example, Dumas and Pelinovsky[26] prove that the log-KdV equation serves as the continuum limit for the monatomic FPUT lattice with Hertzian spring interaction.

1.3. Rigorous results

The main focus of the recent papers[20,23,27] has been to rigorously establish the presence of solutions to the two-component traveling wave problem (1.5) in the neighborhood of the (formal) limiting solutions discussed above. The parameter regimes that have now been treated are depicted in Fig. 2, which we reproduce from Ref. 27, Fig. 2. Each of these regimes has its distinctive features and requires specialized tools and techniques, which we briefly discuss below and in Section 2.

---

[2] In this case both the masses and the spring forces in (1.1) are allowed to vary periodically.
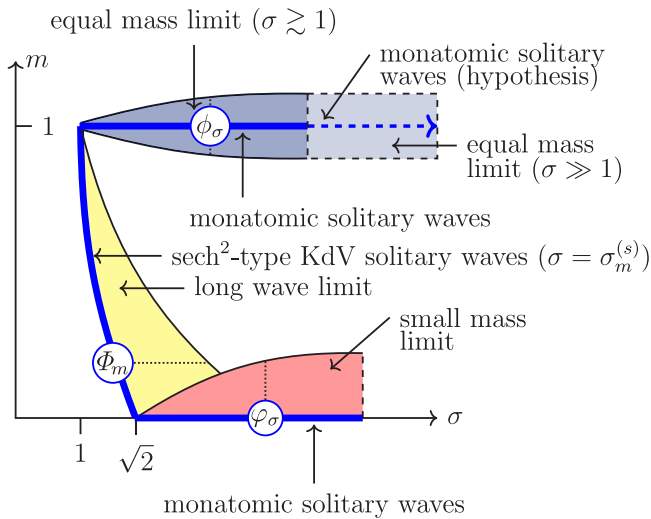
Fig. 2. Bands of rigorously constructed traveling wave solutions for the long wave (yellow), small mass (red), and equal mass (blue) diatomic problems. In general, it is a technical artifact of the various existence proofs in Refs. 20, 23, 27 that the bands collapse as the fixed parameter approaches its own critical value. (For interpretation of the references to color in this figure legend, the reader is referred to the web version of this article.)

1.3.1. Ripples

The common theme in the approaches of Refs. 20, 23, 27 is that one has to give up on the exponential localization of the wave profiles. Stated more informally, the traveling wave Eqs. (1.5) are not generically expected to admit solitary wave solutions. One can interpret this as a manifestation of the purely imaginary spatial eigenvalues associated to the linearization of (1.5) around the zero background state. In contrast to the monatomic setting, this contribution to the essential spectrum cannot be fully removed by applying exponential weight functions. Indeed, the resulting linearization typically has codimension one; see Section 2.3.1.

To fill the resulting gap, one needs to follow Beale's key insight[28] and incorporate the background sinusoidal periodic solutions associated to the eigenvalues mentioned above. At the nonlinear level, this results in an asymptotic "ripple" in the traveling wave profiles at spatial infinity, which destroys their exponential localization.

Quantifying the size of this ripple in terms of the relevant small parameter is an interesting aspect, both from a theoretical and a practical perspective. Indeed, the simulations by Giardetti, Shapiro, Windle, and Wright[29] suggest that the size of the ripple is directly related to the energy loss that the "core" of the wave experiences as it propagates through the lattice. We discuss this issue in detail in Section 5. For now, we simply remark that the (meta-)stability of the diatomic waves constructed in Refs. 20, 23, 27 is a delicate open question.

1.3.2. Nanopterons

The results[3] of Faver and Wright in Ref. 23 show that for fixed $m \in (0, 1)$ there exist long wave solutions to (1.5) for $\sigma \in (\sigma_m^{(s)}, \sigma_m^{(s)} + \delta_m)$ where $\sigma_m^{(s)}$ is the speed of sound from (1.15). Moreover, $\delta_m \to 0$ as $m \to 1^-$. It is unclear what the behavior of δ_m is for $m \to 0$, since the relevant parameter in Ref. 23 is in fact $1/m$ which diverges. The amplitude of the ripple turns out to be small beyond all orders in $\sigma - \sigma_m^{(s)}$, owing to the fact the underlying perturbation from the limiting (scaled) profile Φ_m is singular. Following Boyd's[30] terminology, we refer to the resulting waves as nanopterons; see Fig. 3b for a contrast with the solitary wave.

---

[3] It is also possible to find long wave nanopterons in the spring dimer lattice.[8] This is an FPUT lattice in which the masses are identical but the spring forces alternate.

Similar results due to Hoffman and Wright hold for the small mass regime,[20] but here one fixes $\sigma \gtrsim \sqrt{2}$ (cf. our discussion of (1.11)) and the small parameter is $m > 0$. The difference is that now an underlying solvability condition forces a countable set of mass ratios to be excluded from the analysis. It is unclear whether or not (solitary) waves exist at these ratios, which aggregate at zero.

1.3.3. Micropterons

We considered the equal mass regime in Ref. 27 and established a set of technical conditions under which an (arbitrary) solution (ϕ, σ) to the monatomic problem (1.6) can be extended into the setting $m \approx 1$. A major difference with the previous settings is that the underlying perturbation problem is regular, which allowed us to provide an explicit integral expression to characterize the $\mathcal{O}(m-1)$ behavior of the ripple amplitude; see Section 2.3.3.

We were able to verify these technical conditions for the waves (1.8) by performing a careful expansion in ϵ and examining the leading order terms. However, we strongly suspect that the $\mathcal{O}(m-1)$ coefficient for the ripple amplitude is small beyond all orders in ϵ, which suggests that our expansions cannot rule out that this coefficient vanishes. Nevertheless, we followed the terminology of Boyd[30] and speculatively referred to our constructed solutions as micropterons; see Fig. 3c for a contrast with the nanopteron.

1.3.4. Solitary waves

Although the ripple amplitude is a crucial variable to close the fixed-point arguments in Refs. 20, 23, 27, it could still potentially vanish at certain (σ, m) pairs. The resulting solitary waves can be seen as a lossless mechanism to transport finite-energy states over arbitrary distances. As a consequence, solutions of this type play an important role in many applications and have been extensively studied in many different settings.[4,31–33] It has been conjectured that solitary waves do exist in the diatomic lattice for a countable, discrete set of mass ratios that accumulate at 0; see Refs. 23, 34, 35. We discuss these conjectures in greater detail in Section 1.5.

1.4. Main results

Besides the justification of our "micropteron" terminology from Ref. 27, the main goal of this paper is to numerically examine the full region between the three limiting curves in Fig. 2. In particular, we shed light on the relation between the three types of diatomic waves discussed above by extending them beyond the parameter regimes that were rigorously analyzed in Refs. 20, 23, 27. Hopefully this will set the stage for further analytical work in this intriguing but challenging area; see, e.g., Ref. 23, §7 for a short discussion of the technical obstructions.

Our main technical contribution is that we map out the two-parameter surfaces of micropterons and nanopterons that emerge from the (formal) limiting monatomic profiles at $m = 1$, respectively $m = 0$ (the horizontal solid curves in Fig. 2). This is achieved by numerically solving the MFDE (1.5) for a large number of (σ, m) pairs, using a continuation approach to provide suitable initial conditions. In addition, we numerically evaluate the leading-order coefficient for the micropteron ripple-amplitude and show that it does not vanish.

The main conclusion is that the micropteron and nanopteron surfaces are in fact connected, albeit in a highly nontrivial fashion featuring holes, folds and twists. For example, if one fixes σ and looks at the associated one-dimensional cross-section, the nanopteron and micropteron curves are typically disconnected. Exceptions occur at isolated values of σ and appear to be closely related to the occurrence of double roots as one tracks the ripple amplitude over the curve.

Indeed, as a byproduct of our analysis we uncover several branches of solitary waves. These occur in very narrow bands of m-values that compress as $m \to 0^+$, which hence provides a numerical confirmation of the conjectures from Refs. 34–36 that we discuss below. In order to explore the stability of these solitary waves, we use (an approximation
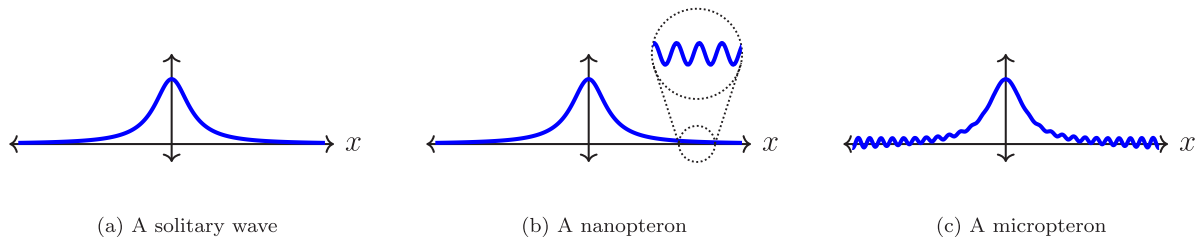
(a) A solitary wave   (b) A nanopteron   (c) A micropteron

Fig. 3. Schematic representation of the three types of traveling waves featured in this paper.

of) one of them as an initial condition for the dynamics of the full FPUT system (1.1). By comparing the resulting behavior with the computations from Ref. 29, we are able to provide strong numerical evidence to suggest that these waves provide stable and robust mechanisms for energy transport.

1.5. Related models

In order to place our results in perspective, we briefly discuss several prior numerical and theoretical studies that are closely related to our setting. These focus on several lattice models that are qualitatively similar to the FPUT system (1.1).

1.5.1. The diatomic Toda lattice

In this setting the spring force in (1.1) is chosen to be the Toda force $F(r) = 1 - e^{-r}$.[37] The extra higher-order terms added to our quadratic expression ensure that the problem is fully integrable. Vainchtein, Starosvetsky, Wright, and Perline[34] study this lattice in the small mass limit. They use a multiscale asymptotic analysis to deduce that small-amplitude traveling waves in the lattice can have oscillations at infinity unless a certain function $\iota(m)$ of the mass ratio m vanishes. They then compute the roots of $\iota(m)$ numerically and conjecture that $\iota(m)$ vanishes for a countable number of mass ratios accumulating at 0. This resembles the FPUT small mass limit in Ref. 20, which could not construct nanopterons at a similar set of mass ratios. Lustri and Porter[35] also work with the diatomic Toda lattice in the small mass limit and use exponential asymptotics to capture the leading order asymptotics of exponentially small terms in solutions. They too calculate a countable number of mass ratios for which these terms vanish and only solitary waves should exist. Lustri[36] uses the same techniques for the diatomic FPUT lattice with our quadratic spring force and makes the same conjecture.

1.5.2. Mass-in-mass lattices

The mass-in-mass (MiM) lattice is a monatomic lattice of "beads" that are "hollow" and contain an additional resonator particle.[4,38] The spring force connecting the beads is typically Hertzian, which is not smooth, unlike the FPUT and Toda forces. Various numerical studies predict the formation of nanopterons in Hertzian lattices.[39–43] Conversely, for a countable number of bead-resonator mass ratios accumulating at 0, Kevrekidis, Stefanov, and Xu[40] prove the existence of solitary wave solutions for the Hertzian MiM lattice. Subsequently, Faver, Goodman, and Wright[44] have found solitary waves at those same mass ratios when the MiM lattice has the quadratic FPUT spring force. For mass ratios small but away from this countable set, Faver[45] has shown the existence of nanopterons, similar to the small mass FPUT limit of Ref. 20.

1.5.3. 1 : N dimers

The "1 : N dimer" is a polyatomic lattice in which one "heavy" mass alternates with N "light" masses. Jayaprakash, Vakakis, and Starosvetsky numerically observe a decreasing sequence of mass ratios that support solitary waves in the 1 : 1[46] and 1 : 2[47] dimers with Hertzian spring forces. With Gendelman, they find in the 1 : 1 dimer a different sequence of mass ratios tending to 0 for which waves asymptote to oscillatory pulses.[48]

1.6. Numerical method

The main technical problem that we face in this paper is that standard path-continuation software packages such as AUTO[49] and PDE2Path[50] cannot be applied to (1.5) on account of the shifts in the arguments. Early numerical work involving MFDEs can be found in Ref. 51, which was continued by Elmer and Van Vleck in the extensive series of papers.[52–56] Results specific to FPUT-type problems can be found in Ref. 44, §4, where the authors use Fourier decompositions to attack the shifted terms.

Our computations here involve the use of a collocation solver based on[52,57] that is able to solve MFDEs on finite intervals. In particular, it can handle general n-component problems of the form

$$\phi'(\xi) = f\Big(\phi(\xi), \phi\big(\xi + \sigma_1(\xi, \phi(\xi))\big), \dots, \phi\big(\xi + \sigma_N(\xi, \phi(\xi))\big)\Big), \tag{1.18}$$

for given functions $f : \mathbb{R}^{n(N+1)} \to \mathbb{R}^n$, $\tau : \mathbb{R} \to \mathbb{R}^n$ and shifts $\sigma_i : \mathbb{R}^{1+n} \to \mathbb{R}$. This is achieved by representing $\phi(\xi)$ on each grid-interval in terms of a standard Runge–Kutta monomial basis, requiring (1.18) to be satisfied at each of the interior Gaussian collocation points.

Various types of boundary conditions can be used to close the system (1.18), which we exploit heavily here in order to ensure that our computed waves have the required "solitary + ripple" structure. Notice that the shifts σ_i may depend on the spatial variable ξ as well as on the function value $\phi(\xi)$ itself. This allows us to compute periodic solutions to MFDEs even when the period is unknown, which is essential for our purposes here.

1.7. Outline

In Section 2 we introduce our computational coordinate system that respects certain important symmetries. In addition, we summarize the mathematical background behind Beale's decomposition procedure for our diatomic waves. We numerically analyze two scalar MFDEs in Section 3 that are related to the monatomic limit, which allows us to compute the leading-order ripple amplitude of our micropterons. The solutions to the full diatomic wave MFDE (1.5) are computed in Section 4, while Section 5 describes our direct simulations of the original FPUT problem (1.1). We close in Section 6 with a brief discussion of possible future research directions.

2. Background

Our goal here is to briefly outline the mathematical background required to appreciate the choices made during our numerical work in later sections. In order to streamline our presentation, we start by introducing the exponentially localized and periodic Sobolev spaces

$$H_q^r := \big\{ f \in H^r \mid \cosh^q(\cdot) f \in H^r \big\},$$
$$H_{\mathrm{per}}^r := \{ f \in H^r([0, 2\pi]) \mid f(0) = f(2\pi) \}, \tag{2.1}$$

using the natural norm

$$\|f\|_{H_q^r} := \big\| \cosh^q(\cdot) f \big\|_{H^r} \tag{2.2}$$

for the weighted spaces. In addition, we define the odd subspaces

$$O_q^r := H_q^r \cap \{\text{odd functions}\}, \qquad O_{\mathrm{per}}^r := H_{\mathrm{per}}^r \cap \{\text{odd functions}\}. \tag{2.3}$$

together with their even counterparts

$$E_q^r := H_q^r \cap \{\text{even functions}\}, \qquad E_{\text{per}}^r := H_{\text{per}}^r \cap \{\text{even functions}\}. \quad (2.4)$$

At times, we restrict the latter even further and consider the "mean-zero" spaces

$$E_{q,0}^r := \left\{ f \in E_q^r \ \Big| \ \int_{-\infty}^{\infty} f(\xi) \, d\xi = 0 \right\},$$

$$E_{\text{per},0}^r := \left\{ f \in E_{\text{per}}^r \ \Big| \ \int_0^{2\pi} f(\xi) \, d\xi = 0 \right\}. \quad (2.5)$$

2.1. Coordinate system

In order to exploit several useful symmetries, it is convenient to introduce new variables for the traveling wave problem. In particular, we introduce a new mass parameter $\mu = 1/m - 1$ to encode the deviation from the equal-mass limit and consider the linear combinations

$$\bar{s}_1 = \frac{\bar{r}_o + \bar{r}_e}{2} \qquad \text{and} \qquad \bar{s}_2 = \frac{\bar{r}_o - \bar{r}_e}{2}. \quad (2.6)$$

Writing $\bar{s} = (\bar{s}_1, \bar{s}_2)$, the diatomic traveling wave MFDE (1.5) can be recast into the form

$$-\sigma^2 \bar{s}'' = \mathcal{D}_1(\mu) \begin{pmatrix} \bar{s}_1 + \bar{s}_1^2 + \bar{s}_2^2 \\ \bar{s}_2 + 2\bar{s}_1 \bar{s}_2 \end{pmatrix}, \quad (2.7)$$

Here we have introduced the linear operator

$$\mathcal{D}_\nu(\mu) := \frac{1}{2} \begin{bmatrix} (2+\mu)(2 - A_\nu) & \mu \delta_\nu \\ -\mu \delta_\nu & (2+\mu)(2 + A_\nu) \end{bmatrix}, \quad (2.8)$$

in which A_ν and δ_ν are the shift operators

$$[A_\nu f](\xi) := f(\xi + \nu) + f(\xi - \nu) \qquad \text{and} \qquad [\delta_\nu f](\xi) := f(\xi + \nu) - f(\xi - \nu). \quad (2.9)$$

It is easy to check that the system (2.7) preserves an "even $\times$ odd" symmetry. More precisely, if $\bar{s}_1$ is even and $\bar{s}_2$ is odd, then the first components of both sides of (2.7) are even (and also mean-zero), while the second components are both odd. A second important symmetry can be readily observed in our original traveling wave problem (1.5). Indeed, this system is invariant under the transformation

$$(\bar{r}_o, \bar{r}_e, m, \sigma) \mapsto (\bar{r}_e, \bar{r}_o, 1/m, \sigma\sqrt{m}). \quad (2.10)$$

We exploit this to perform our numerics on the symmetrized system (2.7) in the bounded regime $\mu \in (-1, 0]$, which corresponds to $m \in [1, \infty)$. Using (2.10) we subsequently transfer these computations back to the regime $m \in (0, 1]$, which we feel is much better suited for discussing and visualizing our results.

2.2. Periodic waves

Here we summarize the procedure used in Refs. 20, 23, 27 to construct the periodic traveling wave solutions that constitute the background ripples of our diatomic waves. We make a few minor changes to the parametrization used in these papers that will facilitate various parts of our subsequent numerics.

2.2.1. The linearized periodic problem

We start by looking for solutions to the linearization of (2.7), which is

$$-\sigma^2 \bar{s}'' = \mathcal{D}_1(\mu)\bar{s}. \quad (2.11)$$

We seek solutions of the form $\bar{s}(\xi) = e^{i\omega\xi}\bar{s}_k$, where $\bar{s}_k \in \mathbb{C}^2$. We find that the vector $\bar{s}_k$ must satisfy the characteristic relation

$$\Delta(\omega; \sigma, \mu)\bar{s}_k = 0,$$

where

$$\Delta(\omega; \sigma, \mu) := \begin{bmatrix} -\sigma^2\omega^2 + (2+\mu)(1 - \cos(\omega)) & i\mu\sin(\omega) \\ -i\mu\sin(\omega) & -\sigma^2\omega^2 + (2+\mu)(1 + \cos(\omega)) \end{bmatrix}. \quad (2.12)$$

Upon introducing the expressions

$$\lambda_\mu^\pm(\omega) := 2 + \mu \pm \sqrt{\mu^2 + 4(1+\mu)\cos^2(\omega)}, \quad (2.13)$$

together with

$$\mathcal{B}_\pm(\omega; \sigma, \mu) := -\sigma^2\omega^2 + \lambda_\mu^\pm(\omega), \quad (2.14)$$

we have the convenient factorization

$$\det\big(\Delta(\omega; \sigma, \mu)\big) = \mathcal{B}_-(\omega; \sigma, \mu)\mathcal{B}_+(\omega; \sigma, \mu). \quad (2.15)$$

For $\mu \geq -1$ we have the useful inequality[427, Eq.(C.1.5)]

$$|(\lambda_\mu^\pm)'(\omega)| \leq 2C_\mu^2|\omega|, \qquad C_\mu := \sqrt{\frac{2(1+\mu)}{2+\mu}}. \quad (2.16)$$

For σ and μ satisfying $\sigma > C_\mu$, this allows us to conclude that $\mathcal{B}_-$ has no zeros other than $\omega = 0$, with the corresponding eigenvector $\Delta(0; \sigma, \mu)(1, 0)^\top = 0$. In addition, the observations

$$\mathcal{B}_+(0; \sigma, \mu) > 0, \qquad \mathcal{B}_+(\infty; \sigma, \mu) = -\infty, \qquad \mathcal{B}_+'\big((0, \infty); \sigma, \mu\big) < 0 \quad (2.17)$$

imply that there is a unique $\omega_{\sigma,\mu} > 0$ with $\mathcal{B}_+(\omega_{\sigma,\mu}; \sigma, \mu) = 0$. The corresponding eigenvector

$$\Delta(\omega_{\sigma,\mu}; \sigma, \mu)\big(v_1^{\sigma,\mu}, v_2^{\sigma,\mu}\big)^\top = 0 \quad (2.18)$$

can be chosen to be continuous in (σ, μ), while satisfying the normalization

$$\big|v_1^{\sigma,\mu}\big|^2 + \big|v_2^{\sigma,\mu}\big|^2 = 1 \qquad \text{and} \qquad \big(v_1^{\sigma,0}, v_2^{\sigma,0}\big) = (0, 1). \quad (2.19)$$

The corresponding solution to the linearization (2.11) is then given by

$$\bar{s}_{\text{lin}}^{\sigma,\mu}(\xi) := \big(v_1^{\sigma,\mu}\cos(\omega_{\sigma,\mu}\xi), v_2^{\sigma,\mu}\sin(\omega_{\sigma,\mu}\xi)\big). \quad (2.20)$$

2.2.2. The full nonlinear periodic problem

One can subsequently construct solutions for the full nonlinear periodic problem (2.7) via a Crandall–Rabinowitz–Zeidler "bifurcation from a simple eigenvalue" argument.[58,59] This provides triplets

$$\big(\bar{p}_1^{\sigma,\mu}[a], \bar{p}_2^{\sigma,\mu}[a], \omega_{\sigma,\mu}[a]\big) \in E_{\text{per},0}^2 \times O_{\text{per}}^2 \times \mathbb{R} \quad (2.21)$$

that are parametrized by the (small) signed amplitude

$$a = \text{sign}\big(\bar{p}_1^{\sigma,\mu}[a](0)v_1^{\sigma,\mu} + (\bar{p}_2^{\sigma,\mu}[a])'(0)v_2^{\sigma,\mu}/\omega_{\sigma,\mu}\big)\sqrt{\|\bar{p}_1^{\sigma,\mu}[a]\|_{L^\infty}^2 + \|\bar{p}_2^{\sigma,\mu}[a]\|_{L^\infty}^2} \quad (2.22)$$

and that yield solutions to (2.7) of the form

$$\bar{s}(\xi) = \bar{p}^{\sigma,\mu}[a](\omega_{\sigma,\mu}[a]\xi) := \big(\bar{p}_1^{\sigma,\mu}[a], \bar{p}_2^{\sigma,\mu}[a]\big)(\omega_{\sigma,\mu}[a]\xi). \quad (2.23)$$

We note that the zero eigenvalue is ruled out by taking $\bar{p}_1^{\sigma,\mu}[a]$ to be a mean-zero function. See Refs. 20, 23, 27 for the details of this construction in the various parameter regimes.

These solutions branch off from the linearized solution in the sense that

$$\bar{p}^{\sigma,\mu}[a] = a\bar{s}_{\text{lin}}^{\sigma,\mu} + \mathcal{O}(a^2) \qquad \text{and} \qquad \omega_{\sigma,\mu}[a] = \omega_{\sigma,\mu} + \mathcal{O}(a). \quad (2.24)$$

Indeed, we view the $\text{sign}(\cdot)$ factor in (2.22) as defining an orientation on a relative to $\bar{s}_{\text{lin}}^{\sigma,\mu}$. Notice in addition that $|a| = \|\bar{p}^{\sigma,\mu}[a]\|_{L^\infty}$, which implies that $|a|$ is genuinely the "amplitude" of the periodic profile $\bar{s}$, which is well-suited for our purposes here.

---

[4] Note that C_μ corresponds with the critical speed $\sigma_m^{(s)}$ defined in (1.15).

We emphasize that our explicit choice (2.22) differs slightly from the definitions in Refs. 20, 23, 27, where the L^∞-norm of the periodic profiles is only $\mathcal{O}(a)$ up to some σ-dependent constants. The equivalence of these different approaches to a follows from the fact that we have Lipschitz-smoothness in a, see Lemma C.1 in Ref. 20 or part (ii) of Lemma C.3 in Ref. 27. We discuss our numerical simulations of these periodic solutions in Section 4.1.

2.3. Micropterons

Here we fix $|\sigma| \gtrsim 1$ and consider masses $m \approx 1$, which allows us to use μ as a small parameter. We set out to find solutions to (2.7) in the vicinity of the pair

$$(\bar{s}_1, \bar{s}_2) = (\phi_\sigma, 0), \tag{2.25}$$

where ϕ_σ solves the monatomic traveling wave problem (1.6).

2.3.1. The linearization at $(\phi_\sigma, 0)$

The linearization of our symmetrized traveling wave problem (2.7) around the pair (2.25) at $\mu = 0$ is the diagonal operator $\mathrm{diag}(\mathcal{H}_\sigma, \mathcal{L}_\sigma)$, whose components are given by

$$\mathcal{H}_\sigma v_1 := \sigma^2 v_1'' + (2 - A_1)[v_1 + 2\phi_\sigma v_1] \qquad \text{and}$$
$$\mathcal{L}_\sigma v_2 := \sigma^2 v_2'' + (2 + A_1)[v_2 + 2\phi_\sigma v_2]. \tag{2.26}$$

The shift operator A_1 was defined in (2.9). The first component $\mathcal{H}_\sigma$ is the linearization of the monatomic traveling wave problem (1.6) at ϕ_σ. For $\sigma \gtrsim 1$ it is known[20,27] that this operator is invertible from E_q^{r+2} to $E_{q,0}^r$ for suitably small q and all $r \geq 0$.

The second component $\mathcal{L}_\sigma$ was analyzed in detail in Ref. 27, where it is shown that $\mathcal{L}_\sigma$ is injective from O_q^{r+2} into O_q^r with

$$\mathrm{Range}(\mathcal{L}_\sigma) = \left\{ g \in O_q^r \ \middle| \ \langle g, \gamma_\sigma \rangle_{L^2} = 0 \right\}. \tag{2.27}$$

Here the odd bounded function γ_σ is a nontrivial solution to the adjoint problem

$$-\sigma^2 \gamma_\sigma'' = (1 + 2\phi_\sigma)(2 + A_1)\gamma_\sigma. \tag{2.28}$$

Recalling the critical frequency $\omega_{\sigma,0}$ from Section 2.2.1, it has the limiting behavior

$$\lim_{\xi \to \infty} |\gamma_\sigma(\xi) - \sin(\omega_{\sigma,0}(\xi + \vartheta_\sigma))| = 0 \tag{2.29}$$

for some asymptotic phase-shift ϑ_σ. More specifically, we have the decomposition

$$\gamma_\sigma(\xi) = \upsilon_\sigma(\xi) + \sin(\omega_{\sigma,0}(\xi + \vartheta_\sigma)) \tag{2.30}$$

in which υ_σ is exponentially localized. We call such a function γ_σ a Jost solution for the adjoint problem (2.28), in the spirit of classical Jost solutions for the Schrödinger operator. We outline our numerical procedure for the computation of these Jost solutions in Section 3.2.

The asymptotic frequency $\omega_{\sigma,0}$ and the asymptotic phase shift ϑ_σ interact in a special way. Recalling the branch (1.7)–(1.8) of solitary waves constructed by Friesecke and Pego, a careful bifurcation analysis that combines MFDE theory with residue calculus[27, Eq. (6.3.14), (6.4.11), App. E.3.2] delivers the expansion

$$\omega_{\sigma_\epsilon,0}\vartheta_{\sigma_\epsilon} = -\frac{\epsilon\omega_{1,0}^2}{8B_+'(\omega_{1,0};1,0)} \int_{-\infty}^{\infty} \mathrm{sech}^2(\xi/2) \, d\xi + \mathcal{O}(\epsilon^2). \tag{2.31}$$

This implies that $\sin(\omega_{\sigma_\epsilon,0}\vartheta_{\sigma_\epsilon}) \neq 0$ for small $\epsilon > 0$, which is essential in the discussion below.

2.3.2. Beale's ansatz

Following Beale,[28] we now search for solutions to the traveling wave problem (2.7) that have the form

$$(\bar{s}_1, \bar{s}_2)(\xi) = (\phi_\sigma, 0)(\xi) + (w_1, w_2)(\xi) + (\bar{p}_1^{\sigma,\mu}[a], \bar{p}_2^{\sigma,\mu}[a])(\xi), \tag{2.32}$$

where we take

$$(w_1, w_2, a) \in E_q^2 \times O_q^2 \times \mathbb{R} \tag{2.33}$$

with $q > 0$ suitably small. One can use the invertibility of $\mathcal{H}_\sigma$ from (2.26) to construct a fixed point equation for the unknown "error" w_1, but obtaining equations for w_2 and the "amplitude" a is more challenging.

The system's second component can be informally written as

$$\mathcal{L}_\sigma w_2 + \mu\chi_\sigma + a\eta_\sigma = \mathcal{O}\big(a^2 + \mu^2 + \|w_1\|_{H_q^2}^2 + \|w_2\|_{H_q^2}^2\big). \tag{2.34}$$

Since the periodic profiles $(\bar{p}_1^{\sigma,\mu}[a], \bar{p}_2^{\sigma,\mu}[a])$ already solve (2.7), the function η_σ can be recognized as the cross-term

$$\eta_\sigma = (2 + A_1)\big[\phi_\sigma \sin(\omega_{\sigma,0}\cdot)\big]. \tag{2.35}$$

In addition, since $(\phi_\sigma, 0)$ satisfies (2.7) at $\mu = 0$, the function χ_σ arises by applying the difference $\mathcal{D}_1(\mu) - \mathcal{D}_1(0)$ to this pair, yielding

$$\chi_\sigma = -\frac{1}{2}\delta_1\big[\phi_\sigma + \phi_\sigma^2\big]. \tag{2.36}$$

2.3.3. The ripple amplitude revealed

The range characterization (2.27) now readily yields

$$a = -K_\sigma \mu + \mathcal{O}(\mu^2), \qquad \text{with} \qquad K_\sigma := \frac{\langle \gamma_\sigma, \chi_\sigma \rangle_{L^2}}{\langle \gamma_\sigma, \eta_\sigma \rangle_{L^2}}, \tag{2.37}$$

which is well-defined for $\sigma = \sigma_\epsilon$ and small $\epsilon > 0$ on account of the remarkable explicit (corrected) identity[27, Eq. 5.3.7]

$$\langle \gamma_\sigma, \eta_\sigma \rangle_{L^2} = -B_+'(\omega_{\sigma,0}; \sigma, 0)\sin(\omega_{\sigma,0}\vartheta_\sigma) \tag{2.38}$$

and the remark following the expansion (2.31).

If $K_\sigma \neq 0$, then the leading-order coefficient for a in (2.38) is nonzero, implying that our ripple's amplitude is only algebraically small in μ. That is, we will have produced a genuine micropteron. It is far from clear, however, whether or not K_σ can ever vanish for a certain choice of σ. Taking $\sigma = \sigma_\epsilon$ and ϕ_{σ_ϵ} to be a near-sonic Friesecke–Pego solitary wave, we might attempt an expansion of K_{σ_ϵ} in powers of ϵ, since there are a host of tight ϵ-estimates on ϕ_{σ_ϵ}.[5,27,60] However, we conjecture that such an expansion will actually reveal that K_{σ_ϵ} is small beyond all algebraic orders of ϵ. Consequently, one of the numerical goals of this paper is to numerically investigate K_σ; see Section 3.

2.4. Nanopterons

In the long wave[23] and small mass[20] limits, the traveling waves are nanopterons, and so the amplitude a of the ripples is small beyond all orders of the relevant small parameter. There is no question, then, of attempting to isolate its leading order behavior as we do for the micropteron. In particular, we do not attempt to compute the analogous Jost solutions that appear in those problems as solutions to certain auxiliary MFDEs.

We do discuss, however, how the formal $m = 0$ solitary waves φ_σ from Section 1.2.2 behave in the $\bar{s}_1$ and $\bar{s}_2$ coordinates. Let φ_σ be an even solitary wave solution of the MFDE (1.11). Since this MFDE is shift-invariant, the profile $\widetilde{\varphi}_\sigma(\xi) := \varphi_\sigma(\xi + 1/4)$ is also a solution. The identities (1.9) and (1.10) tell us that putting

$$\bar{r}_o(\xi) = \widetilde{\varphi}_\sigma(\xi/2) \qquad \text{and} \qquad \bar{r}_e(\xi) = \widetilde{\varphi}_\sigma\big((\xi - 1)/2\big)$$

formally solves the original FPUT traveling wave problem (1.5) at $m = 0$. Then using the change of variables (2.6), we find that these solutions read

$$\bar{s}_1(\xi) = \frac{\varphi_\sigma\big((\xi + 1/2)/2\big) + \varphi_\sigma\big((\xi - 1/2)/2\big)}{2}$$

and

$$\bar{s}_2(\xi) = \frac{\varphi_\sigma\big((\xi + 1/2)/2\big) - \varphi_\sigma\big((\xi - 1/2)/2\big)}{2}.$$

In particular – in contrast to the equal mass limit – the $\bar{s}_2$ component does *not* vanish in the limit $m \downarrow 0$; see for example graph III in Fig. 9.

3. Monatomic simulations

Our goal here is to numerically find solutions to the monatomic traveling wave MFDE (1.6), together with the problem (2.28) that describes the associated Jost solutions. Compared to the discussion in Section 2 above, the main change here is that we do not use the wave speed[5] $\sigma > 1$ to parametrize the waves, but rather introduce a new parameter

$$\kappa \sim \sqrt{8\phi(0)} \tag{3.1}$$

that is a measure for the center amplitude of the wave. This parameter is always supplied *a priori* to our numerical method.

The factor of 8 arises from the estimates for the Frisecke–Pego monatomic solutions in (1.8). Indeed, in view of Ref. 5, Eq. (4.1) this can be seen as an equivalent parametrization for the family (1.7)–(1.8) with the convenient property

$$\epsilon = \kappa + \mathcal{O}(\kappa^2). \tag{3.2}$$

The numerical motivation for this choice is that it is much easier to use fixed boundary conditions for the wave profile. This helps to stabilize the code and also – crucially – prevents convergence to the omnipresent zero solution.

3.1. Wave speed and profile

For fixed $\kappa > 0$, we aim to find a solution

$$\phi(\xi) \sim \kappa^2 \Phi(\kappa\xi), \tag{3.3}$$

to (1.6) by numerically computing the pair (σ, Φ). This scaling is inspired by the limiting behavior (1.8) and allows us to use the same numerical interval for a wide range of values of κ. This enables us to use a continuation approach where we gradually modify κ, without the danger that our solutions become too wide.

In order to find our numerical wave, we introduce a computational coordinate

$$\tau = \kappa\xi \in [0, L] \tag{3.4}$$

for some fixed $L > 0$ and set out to solve the problem

$$-\kappa^2\sigma^2\Phi''(\tau) = \Big[(2 - A_\kappa)(\Phi + \kappa^2\Phi^2)\Big](\tau), \tag{3.5}$$

augmented by the boundary conditions

$$\Phi(0) = \frac{1}{8}, \qquad \Phi'(0) = 0, \qquad \Phi(L) = 0. \tag{3.6}$$

The first condition is related to (3.1), while the second allows us to (virtually) extend Φ to an even function. In particular, we take $\Phi(\tau) = \Phi(-\tau)$ whenever the shifts in (3.5) require an evaluation of Φ at a negative argument.

3.2. Jost solutions

In order to solve (2.28), we write

$$\gamma_\sigma(\xi) \sim \sin\big(\omega_Y(\xi + \theta_Y)\big) + \beta_Y Y(\kappa\xi) \tag{3.7}$$

and set out to numerically compute $(\omega_Y, \theta_Y, \beta_Y, Y)$. The first of these is the solution to the scalar nonlinear problem

$$\sigma^2\omega_Y^2 = 2 + 2\cos(\omega_Y). \tag{3.8}$$

The remainder function Y is characterized by the MFDE

$$-\kappa^2\sigma^2 Y''(\tau) = \Big(1 + 2\kappa^2\Phi(\tau)\Big)\Big(2Y(\tau) + [A_\kappa Y](\tau)\Big) \\ + 2\kappa^2\sigma^2\omega_Y^2\beta_Y^{-1}\Phi(\tau)\sin\big(\omega_Y(\tau/\kappa + \theta_Y)\big), \tag{3.9}$$

augmented by the boundary conditions

$$Y(0) = -\beta_Y^{-1}\sin(\omega_Y\theta_Y), \qquad Y'(0) = 1, \qquad Y(L) = Y'(L) = 0. \tag{3.10}$$

The first of these ensures that γ_σ can be (virtually) extended to an odd function by writing

$$-Y(-\tau) = Y(\tau) + \beta_Y^{-1}\sin\big(\omega_Y(\tau/\kappa + \theta_Y)\big) + \beta_Y^{-1}\sin\big(\omega_Y(-\tau/\kappa + \theta_Y)\big). \tag{3.11}$$

The second boundary condition is a convenient normalization, but it does require us to introduce the extra parameter β_Y in the ansatz (3.7).

3.3. The K_σ coefficient

In order to evaluate the explicit coefficient in (2.37), we introduce the function

$$\Psi^{(\eta)}(\tau) = \Phi(\tau + \kappa)\sin(\omega_Y\tau/\kappa + 1) + 2\Phi(\tau)\sin(\omega_Y\tau/\kappa) \\ + \Phi(\tau - \kappa)\sin(\omega_Y\tau/\kappa - 1), \tag{3.12}$$

together with

$$\Psi^{(\chi)}(\tau) = -\frac{1}{2}\Big[\Phi(\tau + \kappa) + \kappa^2\Phi(\tau + \kappa)^2 - \Phi(\tau - \kappa) - \kappa^2\Phi(\tau - \kappa)^2\Big]. \tag{3.13}$$

This allows us to define the integrals

$$\begin{aligned} \mathcal{I}^{(\eta)} &= 2\kappa\int_0^L \Big[\sin\big(\omega_Y(\tau/\kappa + \theta_Y)\big) + \beta_Y Y(\tau)\Big]\Psi^{(\eta)}(\tau)\,d\tau \\ \mathcal{I}^{(\chi)} &= 2\kappa\int_0^L \Big[\sin\big(\omega_Y(\tau/\kappa + \theta_Y)\big) + \beta_Y Y(\tau)\Big]\Psi^{(\chi)}(\tau)\,d\tau \end{aligned} \tag{3.14}$$

which should be seen as our numerical proxies for the inner products $\langle\gamma_\sigma, \eta_\sigma\rangle_{L^2}$ respectively $\langle\gamma_\sigma, \chi_\sigma\rangle_{L^2}$ that appear in (2.37). In particular, we obtain the numerical prediction

$$K_\sigma \sim -\mathcal{I}^{(\chi)}/\mathcal{I}^{(\eta)}. \tag{3.15}$$

We note that the identity (2.38) implies that we expect to have

$$\mathcal{I}^{(\eta)} \approx -\mathcal{B}'_+(\omega_Y; \sigma, 0)\sin(\omega_Y\theta_Y), \tag{3.16}$$

which we used as an independent monitor for the accuracy of our numerical schemes.

3.4. Implementation

Note that the two scalar differential equations for Φ and Y are both of order two, while there are three free parameters $(\sigma, \beta_Y, \theta_Y)$ that need to be determined. The collocation solver discussed in Ref. 57 hence requires seven boundary conditions, which indeed matches the number supplied in (3.6) and (3.10). We solved the combined system on the interval $[0, L] = [0, 32]$ for a range of values for $\kappa \geq 1/8$. The results for σ and the product $\omega_Y\theta_Y$ can be found in Fig. 4a.

The integrals (3.14) were computed by applying the mid-point rule with 10^6 gridpoints. The resulting values can be found in Fig. 4b. Due to the high-frequency oscillations in the integrand for $\mathcal{I}^{(\chi)}$ that appear as $\kappa \downarrow 0$, the values for this integral become unreliable when κ is too small. For this reason, we restricted the plot to the range $\kappa \geq 0.3$. This cut-off was determined by changing the number of gridpoints used for the integral evaluation and checking whether the computed values remain stable.

3.5. Discussion

Evaluating (1.7), and (2.31) using the reparametrization (3.2) and the observation $\omega_{1,0} \sim 1.478170266$, we arrive at the predictions

$$\omega_Y\vartheta_Y \sim 0.2208053960\kappa + \mathcal{O}(\kappa^2), \qquad \sigma \sim 1 + \frac{1}{24}\kappa^2 + O(\kappa^3). \tag{3.17}$$

These predictions for the phase-shift and wave speed agree remarkably well with our numerics; see Fig. 4a. We also emphasize that we are able to find waves for relatively large values of κ, which (arguably) fall outside of the small-amplitude regime analyzed in Refs. 5, 14.
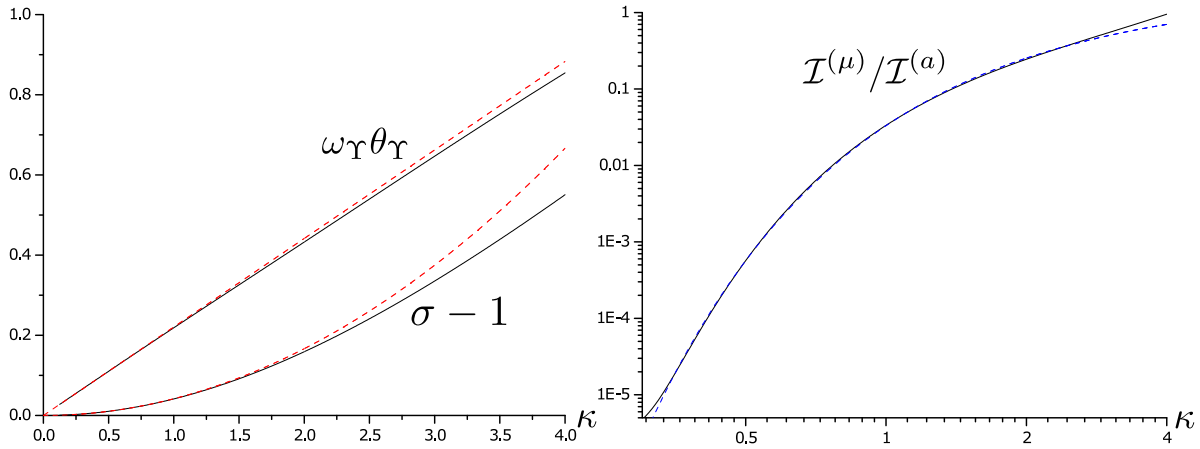
---

[5] From now on we use σ for the wave speed in order to emphasize that it is a numerically computed variable and not a fixed system parameter.

Fig. 4. The left graph visualizes the computed values for the asymptotic phase-shift of the Jost solution and the monatomic wave speed (solid black), together with their leading-order predictions (3.17) (dashed red). The right graph contains our computed values for $-K_\sigma$ (solid black), together with the fit (3.18) (dashed blue). (For interpretation of the references to color in this figure legend, the reader is referred to the web version of this article.)

As discussed in Section 2.3.3, we have no *a priori* predictions for the amplitude coefficient (3.15). To examine this in further detail, we fitted the graph with a function that is exponentially small in κ and found the approximation

$$\mathcal{I}^{(\chi)}/\mathcal{I}^{(\eta)} \approx 1.93756 \exp\left[-4.06704/\kappa\right], \tag{3.18}$$

which agrees quite well with our data points. In particular, we view this as support for our conjecture that K_{σ_ϵ} is small beyond all orders in ϵ. In any case, we now have solid evidence to show that $K_\sigma < 0$ for a wide range of $\sigma > 1$, which in our view justifies the micropteron terminology that we used in Ref. 27.

4. Diatomic simulations

We are now ready to search for solutions of the form (2.32) to the full diatomic wave problem (2.7). We reuse the scaling parameter κ, which now should be interpreted as

$$\kappa \sim \sqrt{8\left(\phi_\sigma(0) + w_1(0)\right)}. \tag{4.1}$$

In particular, this parameter is a measure for the center amplitude of the *solitary* part of the wave, which includes both the known solitary core in Beale's ansatz (2.32) as well as the unknown localized terms, but excludes the background periodic ripple. Since the size of this ripple is zero at $m = 1$ and $m = 0$, this coincides with the parameter κ that we used in the monatomic setting of Section 3.

4.1. Periodic solutions

We first aim to construct candidates for the background ripple by searching for periodic solutions to (2.7) of the form

$$(\bar{s}_1, \bar{s}_2)(\xi) \sim \beta_P(\widetilde{P}_1, \widetilde{P}_2)(\omega_P \xi). \tag{4.2}$$

In particular, in terms of the computational coordinate

$$\widetilde{\tau} = \omega_P \xi \in [0, L], \tag{4.3}$$

we need to solve the problem

$$-\omega_P^2 \sigma^2 \widetilde{P}'' = \mathcal{D}_{\omega_P}(\mu) \begin{pmatrix} \widetilde{P}_1 + \beta_P(\widetilde{P}_1^2 + \widetilde{P}_2^2) \\ \widetilde{P}_2 + 2\beta_P \widetilde{P}_1 \widetilde{P}_2 \end{pmatrix}, \tag{4.4}$$

augmented by the (boundary) conditions

$$\int_0^L \widetilde{P}_1(\widetilde{\tau}) \, d\widetilde{\tau} = 0, \qquad \widetilde{P}_1'(0) = 0, \qquad \widetilde{P}_2(0) = \widetilde{P}_2(L) = 0 \tag{4.5}$$

and the normalization

$$\widetilde{P}_1(0)^2 + \widetilde{P}_2'(0)^2 = 1. \tag{4.6}$$

The conditions (4.5) reflect the choice (2.21), with the understanding that $\widetilde{P}$ is $2L$-periodic. Indeed, we resolve function evaluations outside the interval $[0, L]$ by using the identities

$$\widetilde{P}(\widetilde{\tau} + 2L) = \widetilde{P}(\widetilde{\tau}), \qquad \widetilde{P}_1(-\widetilde{\tau}) = \widetilde{P}_1(\widetilde{\tau}), \qquad \widetilde{P}_2(-\widetilde{\tau}) = -\widetilde{P}_2(\widetilde{\tau}). \tag{4.7}$$

In particular, this means that the triplets (2.21) are represented by

$$\left(\bar{p}_1(\xi), \bar{p}_2(\xi), \omega\right) \sim \left(\beta_P \widetilde{P}_1(L\xi/\pi), \beta_P \widetilde{P}_2(L\xi/\pi), \pi\omega_P/L\right). \tag{4.8}$$

By picking an appropriate initial condition, we can ensure that $\widetilde{P}_2'(0) > 0$ holds whenever $\mu \approx 0$ and β_P is sufficiently small. Our continuation approach subsequently ensures that we maintain the inequality

$$v_1^{\sigma,\mu} \widetilde{P}_1(0) + v_2^{\sigma,\mu} L \widetilde{P}_2'(0)/(\pi\omega_{\sigma,\mu}) > 0 \tag{4.9}$$

throughout all our simulations. In particular, the sign term in the definition (2.22) for the scaled amplitude a agrees with the sign of β_P in view of the correspondence (4.8). In particular, the numerical equivalent of a is given by the new parameter

$$a \sim \alpha_P := \beta_P \sqrt{\|\widetilde{P}_1\|_{L^\infty}^2 + \|\widetilde{P}_2\|_{L^\infty}^2} \tag{4.10}$$

4.2. Diatomic waves

Turning to the full ansatz (2.32), we now look for solutions to (2.7) of the form

$$(\bar{s}_1, \bar{s}_2)(\xi) \sim \kappa^2 V(\kappa\xi) + \beta_P P(\kappa\xi). \tag{4.11}$$

Here we have introduced the reparametrization

$$P(\tau) = \widetilde{P}(\omega_P \tau/\kappa) \tag{4.12}$$

in order to recast the system in terms of the usual coordinate

$$\tau = \kappa\xi \in [0, L]. \tag{4.13}$$

Note that the solitary component $V = (V_1, V_2)$ represents the entire solitary "core" of Beale's ansatz (2.32). This consists of the "known" localized term $(\phi_\sigma, 0)$ and the "unknown error" term (w_1, w_2), in line with our interpretation of the parameter κ in (4.1). In particular, we do not incorporate the monatomic waves from Section 3 because this would only add to the complexity of the numerical procedure.

The full solitary component V should now satisfy the system

$$-\kappa^2 \sigma^2 V'' = \mathcal{D}_\kappa(\mu) \begin{pmatrix} V_1 + \kappa(V_1^2 + V_2^2) + 2\beta_P(V_1 P_1 + V_2 P_2) \\ V_2 + 2\kappa V_1 V_2 + 2\beta_P(V_1 P_2 + V_2 P_1) \end{pmatrix}, \tag{4.14}$$

augmented by the boundary conditions

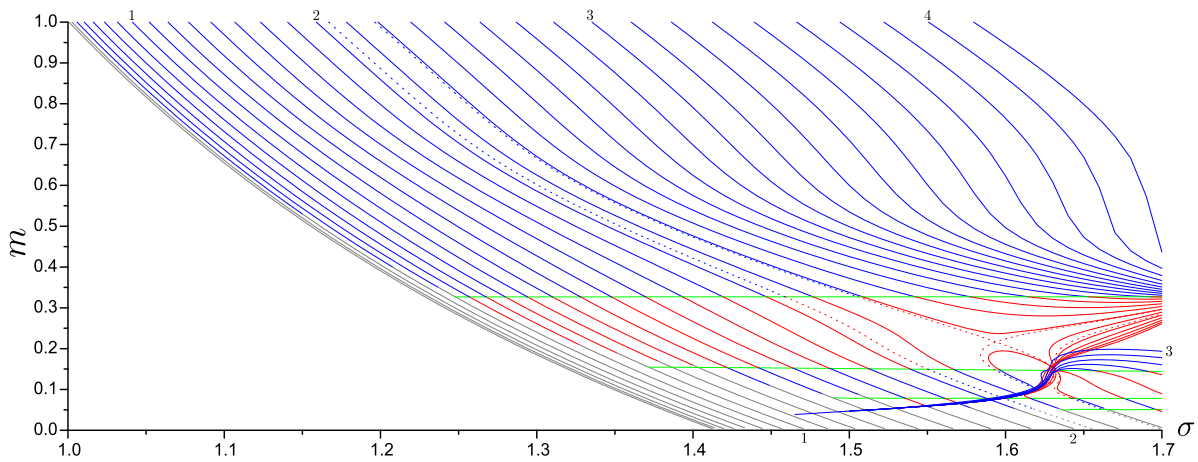$$V_1(0) = \frac{1}{8}, \qquad V_1'(0) = 0, \qquad V_2(0) = 0, \qquad V_1(L) = 0,$$

Fig. 5. Overview of several iso-κ curves where diatomic waves exist. The small integers denote the κ values, while the dashed separatrices correspond to the special values (4.16). The color codes are described in Section 4.3. Notice that the green branches of solitary waves and the blue fold curve terminate for technical reasons, but in principle extend further into the gray "small-ripple" regime. (For interpretation of the references to color in this figure legend, the reader is referred to the web version of this article.)
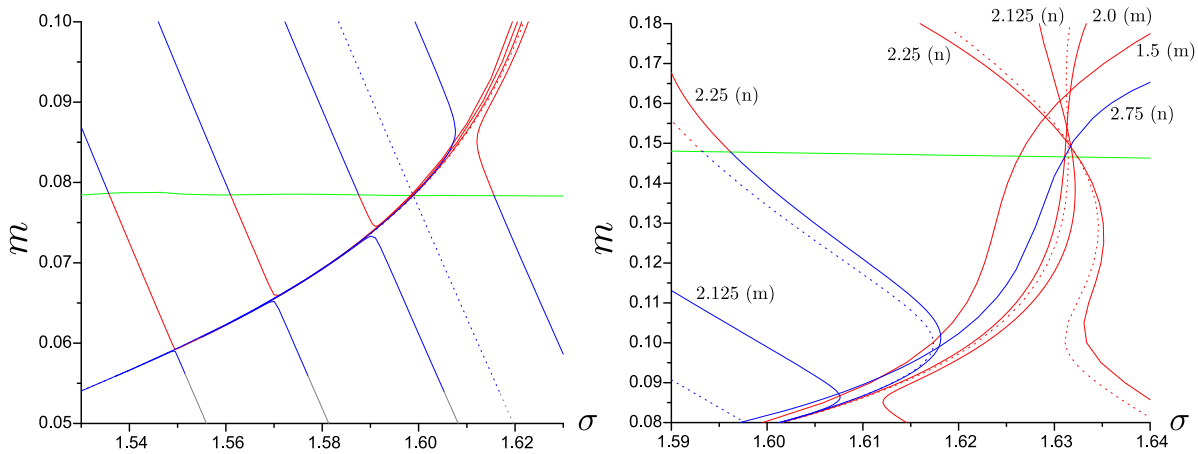

Fig. 6. Two zoomed views of interesting regions in Fig. 5. For presentation purposes, we only plot a subset of the iso-κ curves. The small numbers next to the curves in the right panel correspond to κ, while (n) and (m) stand for the nanopteron respectively micropteron branch. (For interpretation of the references to color in this figure legend, the reader is referred to the web version of this article.)

$$V_2(L) = V_2'(L) = 0. \tag{4.15}$$

The first three of these allow us to extend V_1 and V_2 as even respectively odd functions, allowing evaluations with $\tau < 0$ to be resolved. Evaluations with $\tau > L$ are set to zero, while evaluations of P outside of $[0, L]$ are performed using (4.7).

4.3. Implementation

For each individual run of the collocation solver, we fix the parameter $\kappa > 0$ together with one of the variables from the set $\{\sigma, \mu, \beta_P\}$. The remaining two variables then need to be computed, along with ω_P and the functions (V_1, V_2, P_1, P_2). Since the latter all satisfy second-order MFDEs, our solver requires $4 \times 2 + 3 = 11$ boundary conditions, which corresponds with the eleven boundary conditions formulated above. This freedom to choose the second fixed parameter is essential for our continuation approach, since it allows us to move past fold points by switching our choice.

In Fig. 5 we consider several values of $\kappa \in \mathbb{N}/8$ and trace out the corresponding curve(s) in the (σ, m) landscape where we were able to find diatomic solitary waves for the chosen value of κ. In addition, we use broken lines to plot these curves for the special values

$$\kappa \in \{2.0515, 2.237567\}, \tag{4.16}$$

where the behavior of these curves experiences a structural change. These values were determined by an unsophisticated bisection approach. In Fig. 6 we provide a zoomed-in view of two interesting areas near the folds, which we discuss in further detail below.

We use the ripple-amplitude α_P to color the curves. In principle, we use blue and red for positive respectively negatives values. However, we pay special attention to the regime where the ripple amplitude is at least a factor of 10^{-5} smaller than the center amplitude of the solitary component, i.e., where

$$|\alpha_P| < 10^{-5}\kappa^2 V_1(0) = 10^{-5}\frac{\kappa^2}{8}. \tag{4.17}$$

In particular, whenever (4.17) holds for an interval of μ of length at least 0.01, we color the entire segment of the curve where it holds gray. In this so-called "small-ripple" regime it is hard to distinguish numerically between positive and negative values of α_P, as can be seen from the top-left graphs in Figs. 7–9.

This problem is further illustrated by the green curves in Figs. 5 and 6, which we computed by fixing $\alpha_P = \beta_P = 0$ and performing a κ scan. In particular, the diatomic waves along these curves are in fact solitary waves. We were only able to continue these branches slightly into the "small-ripple" regime, after which the scheme failed to converge. We emphasize that this does not necessarily mean that these branches terminate.
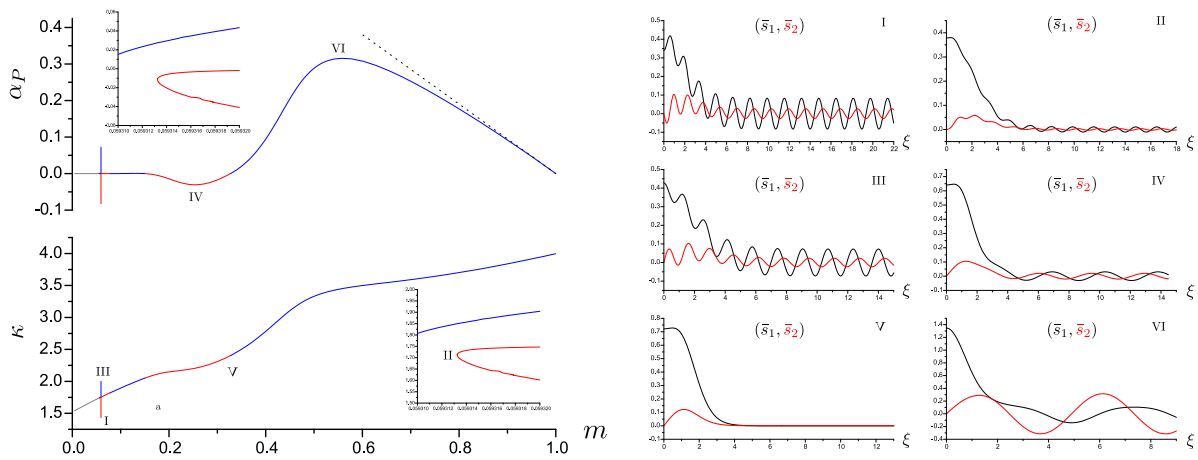
Fig. 7. The left graphs contain vertical cross-sections of Fig. 5 with $\sigma = 1.55$. The dashed line represents the leading-order ripple-amplitude prediction (2.37) computed with (3.15), while the insets zoom in on the region where the micropteron and nanopteron branches approach each other. The six graphs on the right contain the solution profiles associated to the special points I through VI marked on the left graphs. (For interpretation of the references to color in this figure legend, the reader is referred to the web version of this article.)
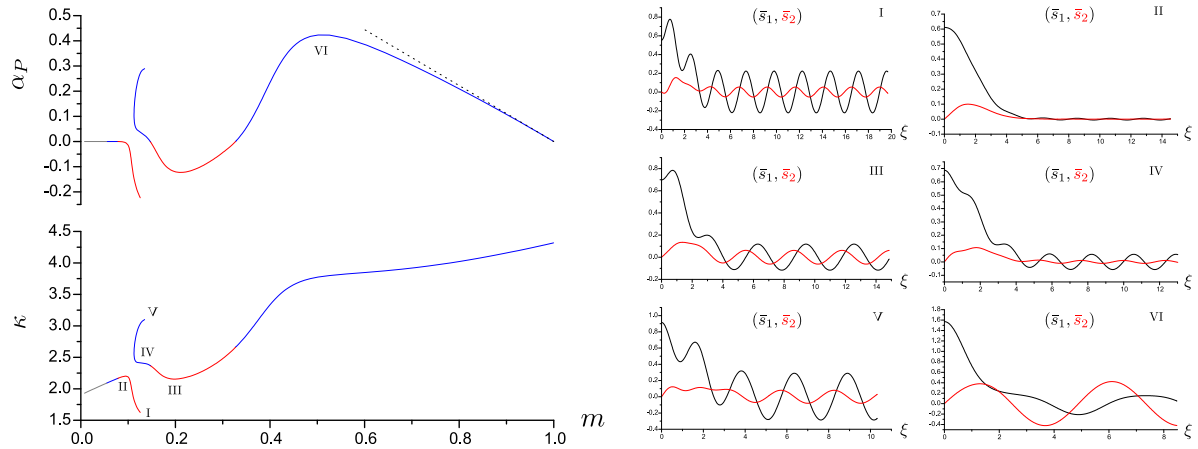

Fig. 8. Cross-sections and solution profiles at $\sigma = 1.625$; see Fig. 7 for more information. (For interpretation of the references to color in this figure legend, the reader is referred to the web version of this article.)

Fig. 9. Cross-sections and solution profiles at $\sigma = 1.65$; see Fig. 7 for more information. (For interpretation of the references to color in this figure legend, the reader is referred to the web version of this article.)
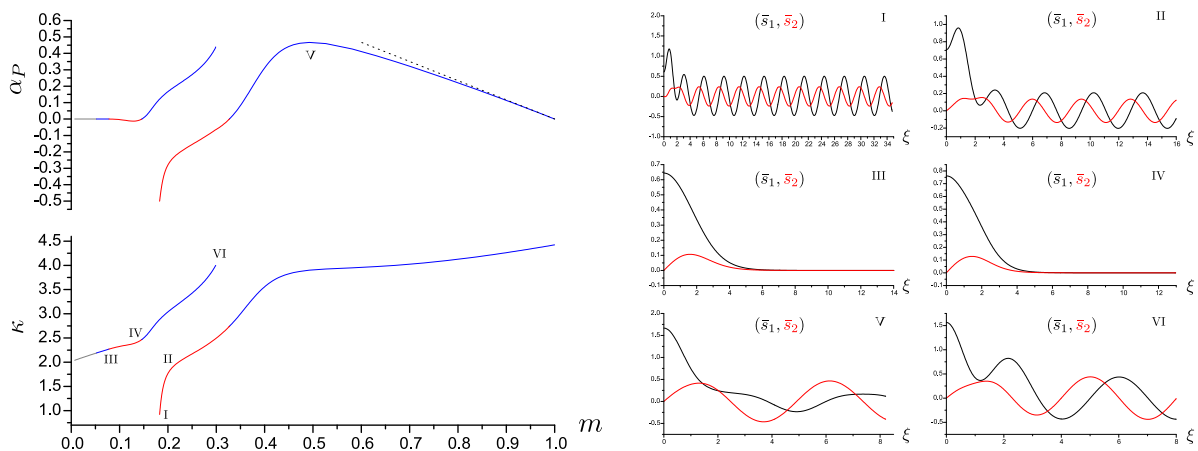
The bottom-left graphs in Figs. 7–9 can be seen as vertical cross-sections of Fig. 5. Indeed, they were obtained by fixing the wave speed σ and performing (several) κ-scans, using continuation to find appropriate initial solutions. Besides κ, these figures also visualize α_P as a function of m.

As can be seen, in these cross-sections we were unable to access regions with $\kappa \leq 1$. We suspect that this is a consequence of the increasing number of mesh intervals that are required to resolve the oscillations in the solitary component V, which leads to memory issues. Indeed, at present our software uses legacy 32-bit code that limits the amount

of accessible memory to roughly 4 Gb. Due to the (relatively) large number of components in the system and the non-standard structure of the underlying matrices caused by the shifted arguments in the MFDE (1.5), this limit is reached much sooner than one would encounter when solving ODEs.

For similar reasons, we have not been able to extend the (blue) fold curve that presently terminates at $(\sigma, m) = (1.46518, 0.038711)$ in Fig. 5 to smaller values of σ. More precisely, we could not continue the $\kappa = 1.5$ "nanopteron" branch (emanating from $m = 0$) past this point. On the other hand, for smaller values of κ we were unable to resolve the "turn" where the "micropteron" (emanating from $m = 1$) and "nanopteron" branches move away from each other. Indeed, Fig. 6a clearly shows that these "turn regions" become increasingly thin as κ decreases. Increasingly delicate techniques are therefore required to prevent the continuation procedure from simply jumping between the two branches.

4.4. Discussion

The overview in Fig. 5 and the iso-σ cross-sections in Figs. 7–9 clearly show that one cannot simply speak about separate "micropteron" and "nanopteron" surfaces. For example, the iso-κ curves converge precisely to the critical speed-of-sound $\sigma_m^{(s)}$ defined in (1.15) for the long-wave nanopterons as $\kappa \downarrow 0$. In addition, the curves emanating from $m = 1$ and $m = 0$ are connected together in a complicated fashion.

However, if one fixes either of the parameters κ or σ, the resulting one-dimensional cross-sections do generically consist of two separate curves. We have identified several exceptions in Figs. 5 and 6 and conjecture that there is a countable set of such special values that accumulates at $\kappa = 0$ respectively $\sigma = \sqrt{2}$.

In order to support this conjecture, let us consider the region where $\sigma \leq 1.61$ and $m \leq 0.08$, where a large set of iso-κ curves converge together to form a narrow "fold-region" that becomes increasingly thin as σ decreases. Depending on the sign of α_P, the "micropteron" and "nanopteron" curves seem to bend sharply to the left or right as this fold is approached. Our observations for $\kappa = 2.0515$ suggest that a switch in direction occurs precisely when the "micropteron" and "nanopteron" curves connect to each other and the associated α_P function admits a double root when passing through the "connection" point at $m \sim 0.0784$. We found faint numerical hints of a second such direction switch when the fold crosses through $m \sim 0.05$, but did not have the numerical resolution to fully resolve this bifurcation.

In particular, we suspect that the (green) branches of solitary waves play an important role as they contain the "crossing-points" between the nanopteron and micropteron subsurfaces. Although we had trouble tracking them deep into the "small-ripple" regime, we did find several of these branches. They indeed appear to accumulate in the small-mass regime, lending credence to the conjectures discussed above. It interesting to note that these branches are not horizontal, i.e., the value of m changes gradually as σ is varied. This is especially true for the $m \sim 0.15$ branch, which has a relatively substantial slope.

We believe that the fold-region discussed above continues into the corner $(\sigma, m) = (\sqrt{2}, 0)$, admitting a countable number of connection switches as it crosses through the branches of solitary waves. In our opinion it would be extremely interesting to perform a theoretical analysis near this corner. One could proceed by examining how the long-wave techniques developed in Ref. 23 and the small-mass argument discussed in Ref. 20 break down as their auxiliary parameters approach the limits $1/m \to \infty$ respectively $\sigma \to \sqrt{2}$. Combining these approaches with the techniques developed by Lombardi[61] to uncover exponentially small phenomena could hopefully lead to some useful insights here.

A second (related) question that deserves further attention concerns the behavior of the "micropteron" and "nanopteron" branches after their "near-collision" events; see the left graphs in Figs. 7–9. It appears

that the red branches where $\alpha_P < 0$ suffer a collapse in the amplitude of the solitary component of the wave, i.e., $\kappa \downarrow 0$, potentially converging to a branch of purely periodic ripples. It is unclear what happens to the blue branches, where both the ripple amplitude and the core amplitude experience significant growth.

5. Stability of solitary waves

In order to gain some insight into the stability of the solitary waves that we found in Section 4, we performed a series of direct time-integrations of the full FPUT system. For our purposes here, it is advantageous to introduce a new momentum variable $p_j = \dot{x}_j$ and reformulate (1.1) as

$$\dot{r}_j = p_{j+1} - p_j, \qquad m_j \dot{p}_j = F(r_j) - F(r_{j-1}), \qquad (5.1)$$

recalling that the masses are given by (1.2). The advantage of these coordinates is that the energy function

$$\mathcal{E}_\Lambda = \sum_{j \in \Lambda} \left[\frac{1}{2} m_j p_j^2 + \frac{1}{2} r_j^2 + \frac{1}{3} r_j^3 \right] \qquad (5.2)$$

is conserved in time upon taking $\Lambda = \mathbb{Z}$, but also easy to compute for any subset $\Lambda \subset \mathbb{Z}$. In general, diatomic waves of the form (2.32) will have infinite energy on account of the periodic background state. However, for solitary waves (where $a = 0$) the energy is finite, since the pair (w_1, w_2) is exponentially localized.

In the monatomic case $m = 1$, Friesecke and Pego[15–17] established that the traveling wave solution $r_j(t) = \phi_{\sigma_\epsilon}(j - \sigma_\epsilon t)$ is stable under the dynamics of (5.1) whenever $\epsilon > 0$ is sufficiently small. In particular, any "sufficiently small" initial perturbation to the wave will die out over time, although the speed and phase of the wave could be slightly changed. In practice, one sees that perturbations produce a small wrinkle that separates itself from the core of the wave and travels at a slower speed.

By contrast, the stability properties of diatomic traveling waves are poorly understood at present. The main obstruction is that one has to control the fluctuations caused by the ripples; see, e.g., Ref. 62 for a discussion of the complications that arise in the stability analysis of water wave nanopterons. Indeed, the numerical results from Ref. 29 – which use the suitably scaled solitary KdV profiles (1.17) as initial conditions for (5.1) – clearly indicate that ripples will appear that *do not* detach from the core of the wave. Instead, they slowly drain energy from this core, causing the amplitude to decay over time. Nevertheless, these structures persist over much longer timescales than those that can be extracted by using amplitude equations. For example, Gaison, Moskow, Wright and Zhang[25] consider a general class of polyatomic lattices that includes our case here and show that the relevant KdV reductions that govern the long-wave limit remain valid over algebraically long timescales.

In order to examine these issues, we introduce the time-dependent set of gridpoints

$$\Lambda_{\text{core}}(t) = \left\{ j \in \mathbb{Z} \mid \left| j - \operatorname{argmax} |r_j(t)| \right| \leq 20 \right\} \qquad (5.3)$$

that is centered around the peak of a solution to (5.1). Our goal is to monitor the behavior of the loss function

$$\Gamma_{\text{core}}(t) = \frac{\mathcal{E}_{\Lambda_{\text{core}}(100)} - \mathcal{E}_{\Lambda_{\text{core}}(t)}}{\mathcal{E}_{\Lambda_{\text{core}}(100)}} \qquad (5.4)$$

for various solutions resembling diatomic and monatomic waves. This fraction measures the relative energy loss in the core of the wave compared to the situation at $t = 100$, allowing sufficient time for initial transients to decay.

We deliberately do not use the peak amplitude of the wave here, since at each point in time only a discrete subset of the underlying smooth waveprofile is "sampled" on the lattice. We do however keep track of the outer amplitude

$$\mathcal{A}_{\text{out}}(t) = \max_{j \notin \Lambda_{\text{core}}(t)} |r_j(t)| \qquad (5.5)$$
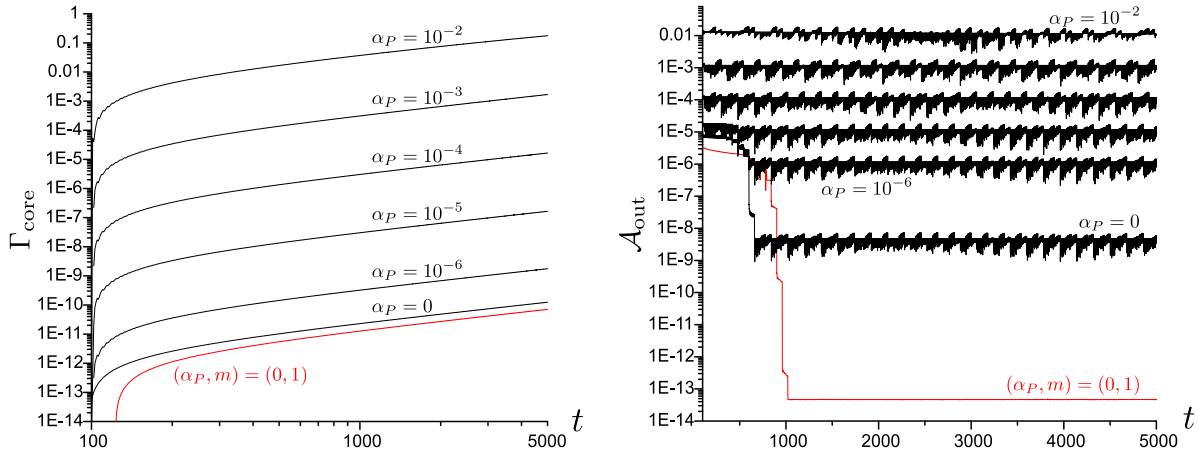
Fig. 10. Behavior of the core energy loss (5.4) and the outer amplitude (5.5) for several simulations of the full FPUT system (5.1). The values of α_P correspond with the initial conditions (5.6). The red curves represent the monatomic equal-mass solitary wave at $\kappa = 5/2$. (For interpretation of the references to color in this figure legend, the reader is referred to the web version of this article.)

as a secondary measure.

5.1. Implementation

We use the `solve_ivp` method from the SciPy package for Python to integrate the problem (5.1) on the grid $\Lambda_{\text{grid}} = \{1, 2, \ldots, 400\}$. In particular, we set both r and p to zero outside this grid. We consider six separate initial conditions, which each consist of the solitary part (i.e., the pair (V_1, V_2)) of one of the diatomic waves computed in Section 4. More precisely, we pick $\kappa = 5/2$ and consider the waves associated to the pairs

$$(\alpha_P, m) \in \{(10^{-2}, 0.33797458), (10^{-3}, 0.32800968), (10^{-4}, 0.32711659),$$
$$(10^{-5}, 0.32702829), (10^{-6}, 0.32701947), (0, 0.32701849)\},$$
$$(5.6)$$

which have wave speeds in the range $\sigma \in [1.563, 1.578]$. For comparison purposes, we also considered the monatomic wave $(\alpha_P, m) = (0, 1)$, again with $\kappa = 5/2$. The results of these simulations can be found in Fig. 10, where we plot the evolution of the core energy loss $\Gamma_{\text{core}}(t)$ and the outer amplitude $\mathcal{A}_{\text{out}}(t)$.

We note that the `solve_ivp` routine utilizes the RK4 scheme with an adaptive step-size Δt. We monitored the energy $\mathcal{E}_{\Lambda_{\text{grid}}}$ over the full grid in order to keep track of potential discretization errors introduced by the scheme. This turned out to be a crucial precaution, because the step-size automatically chosen by `solve_ivp` led to unacceptable fluctuations in this energy. To prevent this, we manually enforced the step-size restriction $\Delta t \leq 10^{-3}$, which is considerably lower than in Ref. 29. We note that an alternative approach could be to use symplectic energy-preserving schemes as described in Ref. 63, but we believe that this is too cumbersome for our illustrative purposes here.

We run our simulations for $t \in [0, 5000]$, which means that the waves will have shifted roughly 7850 lattice points to the left. Since this considerably exceeds the size of our grid, we need to account for this movement in a special fashion. Our choice here is to use a "windowing" procedure, where we shift the solution rightwards to recenter the peak at the center of the computation grid, filling r and p with zeros at the empty positions on the left side of the grid. In order to prevent large discontinuities arising from the sudden cutoff at the right end of the grid, we apply the pointwise multiplication

$$(r_i, p_i) \mapsto e^{-y_i^2/(1-y_i^2)}(r_i, p_i), \qquad y_i = \max\{(i - 300)/100, 0\}. \quad (5.7)$$

In particular, we use a smooth cut-off function to gradually scale the solution on the right 25% of the lattice sites down to zero. In contrast to the approach in Ref. 29, we only perform this recentering and

windowing procedure once per sixty units of time. We emphasize that other methods are available to deal with this problem, such as the freezing technique developed by Beyn and coworkers.[64]

5.2. Discussion

Naturally, due to discretization effects and rounding issues there will always be some energy leakage as a numerical wave moves through the lattice. In addition, sampling and interpolation errors occur when passing initial conditions from the boundary value problem solver used in Section 4 to the FPUT simulator discussed here. This causes the initial transient behavior and subsequent slow energy leakage that is displayed in Fig. 10 for the monatomic wave. We use this as a baseline to interpret the behavior of the diatomic waves.

The results in Fig. 10a show that our numerical diatomic solitary wave loses energy at an extremely slow rate that is comparable to its monatomic counterpart. In addition, the initial transient clearly indicates that our diatomic solitary wave is stable in a certain sense. Notice furthermore that this coherence disappears rapidly if the mass m is disturbed. Indeed, the size of the ripple-amplitude α_P is clearly correlated with the speed at which the core of the wave loses energy.

We reiterate that the results in Ref. 29 already suggest that – in general – diatomic waves decay at rates that are much slower that those suggested by their formal KdV approximations. This effect is amplified in the small-amplitude regime, where[29] contains examples that display practically no decay on very long time-scales. For this reason, we consider the relatively large value $\kappa = 5/2$, which through the parameter translation

$$(\kappa, m) \sim (\sqrt{24\tilde{\epsilon}}, 1/m_2) \tag{5.8}$$

means that our results should be compared to the results in Ref. 29 with $\tilde{\epsilon} = 1/2$ and $m_2 = \pi$, which were the largest values that the authors consider. In particular, our results should be compared with the top-left plot in Ref. 29, Fig. 8, noting that our time-interval corresponds roughly with $[0, 10^4]$ in that figure.

The conclusion from this comparison is that the observed "outer amplitude" $\mathcal{A}_{\text{out}}$ for our diatomic solitary waves is orders of magnitude smaller than the wakes observed in Ref. 29. The loss function Γ_{core} exhibits a similar scale reduction, although this is harder to read-off from the figure due to the smaller numbers. Together, we feel that these observations strongly suggest that the $m \sim 0.33$ branch of solitary waves found in Section 4 are indeed solitary and stable, providing a robust transport mechanism in the diatomic setting.

6. Future directions

In this paper we considered the numerical behavior of diatomic FPUT lattices with the quadratic spring force $F(r) = r + r^2$. The MiM lattice is a natural candidate for future investigations of this sort, since its traveling wave equations are MFDEs similar to (1.5), and since it possesses a sturdy theory of solitary waves[40,44] and nanopterons[45] in the small bead-resonator mass limit. In particular, from Ref. 40 and Ref. 44 there is a simple, explicit formula for those mass ratios accumulating at 0 at which the MiM lattice has solitary waves. It is also possible to pose a "stiff internal spring" limit for the MiM lattice, in which the bead-resonator spring becomes arbitrarily stiff, and the MiM lattice again reduces to a monatomic FPUT lattice. Solitary waves are known to exist in this limit, too,[44] and one expects nanopterons there was well. There could be an interesting parameter overlap, similar to the regimes in Fig. 2, in which the bead-resonator spring force is extremely stiff and the bead-resonator mass ratio is extremely small.

While we numerically simulated periodic solutions to FPUT lattices, we did not consider how different families of periodics relate to each other, in the spirit of the full nanopterons and micropterons in Fig. 2. Friesecke and Mikikits-Leitner[65] construct periodic traveling waves in the long wave limit for monatomic lattices. Do these have any connection to the periodic waves in diatomic lattices from Ref. 23 when the mass ratio is close to 0 or 1? We also mention that Betti and Pelinovsky study periodic waves in a diatomic lattice with Hertzian spring forces.[66] They begin with periodic solutions in the small mass limit but manage to extend them numerically to the equal mass limit. For a given wave speed σ, is it possible to extend the FPUT periodics in the same way, from $m \approx 0$ to $m \approx 1$?

Last, in more general polyatomic FPUT lattices, in which both the masses and the spring forces repeat with some finite periodicity, it is known that solutions to the equations of motion with suitably scaled initial data look like KdV sech^2-type solitary waves over long times.[25] However, it is not yet known whether these solitary wave approximations persist for all time, as in the monatomic lattice, evolve into nanopterons, as in the diatomic lattice, or become something else entirely. In a more complicated polyatomic lattice, there are fewer opportunities for a natural "material" limit, like the small or equal mass regimes, to reduce the polyatomic lattice to monatomic. Nonetheless, our numerical methods could give insight into the formation of, at least, solitary waves in the long wave polyatomic limit.

CRediT authorship contribution statement

Timothy E. Faver: Conception and design of study, Analysis and/or interpretation of data, Writing – original draft, Writing – review & editing. **Hermen Jan Hupkes:** Conception and design of study, Analysis and/or interpretation of data, Writing – original draft, Writing – review & editing.

Acknowledgments

References

1. Fermi E, Pasta J, Ulam S. Studies of nonlinear problems. *Lect Appl Math*. 1955;12:143–156.
2. Dauxois T. Fermi, Pasta, Ulam, and a mysterious lady. *Phys Today*. 2008;61(1):55–57.
3. Brillouin L. *Wave Propagation in Periodic Structures*. New York, NY: Dover Phoenix Editions; 1953.
4. Kevrekidis PG. Non-linear waves in lattices: past, present, future. *IMA J Appl Math*. 2011;76(3):389–423.
5. Friesecke G, Pego RL. Solitary waves on FPU lattices. I. Qualitative properties, renormalization and continuum limit. *Nonlinearity*. 1999;12(6):1601–1627.
6. Herrmann M, Matthies K. Asymptotic formulas for solitary waves in the high-energy limit of FPU-type chains. *Nonlinearity*. 2015;28:2767–2789.
7. Pankov A. *Travelling Waves and Periodic Oscillations in Fermi-Pasta-Ulam Lattices*. Singapore: Imperial College Press; 2005.
8. Faver TE. Nanopteron-stegoton traveling waves in spring dimer Fermi-Pasta-Ulam-Tsingou lattices. *Quart Appl Math*. 2020;78:363–429.
9. Mallet-Paret J. The global structure of traveling waves in spatially discrete dynamical systems. *J Dynam Differential Equations*. 1999;11:49–128.
10. Chen X, Guo J-S, Wu C-C. Traveling waves in discrete periodic media for bistable dynamics. *Arch Ration Mech Anal*. 2008;189(2):189–236.
11. Hupkes HJ, Sandstede B. Travelling pulse solutions for the discrete FitzHugh-Nagumo system. *SIAM J Appl Dyn Syst*. 2010;9:827–882.
12. Keener JP. Propagation and its failure in coupled systems of discrete excitable cells. *SIAM J Appl Math*. 1987;47:556–572.
13. Hupkes HJ, Morelli L, Schouten-Straatman W, Vleck E. Traveling waves and pattern formation for spatially discrete bistable reaction-diffusion equations. In: Bohner M, Siegmund S, Šimon Hilscher R, Stehlík P, eds. *Difference Equations and Discrete Dynamical Systems with Applications*. 2020:55–112.
14. Friesecke G, Wattis JAD. Existence theorem for solitary waves on lattices. *Comm Math Phys*. 1994;161(2):391–418.
15. Friesecke G, Pego RL. Solitary waves on FPU lattices. II. Linear implies nonlinear stability. *Nonlinearity*. 2002;15(4):1343–1359.
16. Friesecke G, Pego RL. Solitary waves on Fermi-Pasta-Ulam lattices. III. Howland-type Floquet theory. *Nonlinearity*. 2004;17(1):207–227.
17. Friesecke G, Pego RL. Solitary waves on Fermi-Pasta-Ulam lattices. IV. Proof of stability at low energy. *Nonlinearity*. 2004;17(1):229–251.
18. Herrmann M, Matthies K. Uniqueness of solitary waves in the high-energy limit of FPU-type chains. In: Gurevich P, Hell J, Sandstede B, Scheel A, eds. *Patterns of Dynamics*. Springer; 2017:3–15. In: Springer Proceedings in Mathematics & Statistics; vol. 205.
19. Herrmann M, Matthies K. Stability of high-energy solitary waves in Fermi-Pasta-Ulam-Tsingou chains. *Trans Amer Math Soc*. 2019;372:3425–3486.
20. Hoffman A, Wright JD. Nanopteron solutions of diatomic Fermi-Pasta-Ulam-Tsingou lattices with small mass-ratio. *Physica D*. 2017;358:33–59.
21. Pelinovsky DE, Schneider G. The monoatomic FPU system as a limit of a diatomic FPU system. *Appl Math Lett*. 2020;107:106387.
22. Schneider G, Wayne CE. The long-wave limit for the water wave problem I. The case of zero surface tension. *Comm Pure Appl Math*. 2000;LIII:1475–1535.
23. Faver TE, Wright JD. Exact diatomic Fermi-Pasta-Ulam-Tsingou solitary waves with optical band ripples at infinity. *SIAM J Math Anal*. 2018;50(1):182–250.
24. Schneider G, Wayne CE. Counter-propagating waves on fluid surfaces and the continuum limit of the Fermi-Pasta-Ulam model. In: *International Conference on Differential Equations*. River Edge, NJ: World Scientific; 2000:390–404.
25. Gaison J, Moskow S, Wright JD, Zhang Q. Approximation of polyatomic FPU lattices by KdV equations. *Multiscale Model Simul*. 2014;12(3):953–995.
26. Dumas E, Pelinovsky DE. Justification of the log-KdV equation in granular chains: the case of precompression. *SIAM J Math Anal*. 2014;46:4075–4103.
27. Faver TE, Hupkes HJ. Micropteron traveling waves in diatomic Fermi-Pasta-Ulam-Tsingou lattices under the equal mass limit. *Physica D*. 2020;410:132538.
28. Beale JT. Exact solitary water waves with capillary ripples at infinity. *Comm Pure Appl Math*. 1991;44(2):211–257.
29. Giardetti N, Shapiro A, Windle S, Wright JD. Metastability of solitary waves in diatomic FPUT lattices. *Math Eng*. 2019;1(3):419–433.
30. Boyd JP. *Weakly Nonlocal Solitary Waves and beyond-All-Orders Asymptotics*. Dordrecht, The Netherlands: Kluwer Academic Publishers; 1998. Mathematics and its Applications; vol. 442.
31. Sandstede B. Stability of travelling waves. In: Fiedler B, ed. *Handbook of Dynamical Systems, Vol. 2*. Elsevier; 2002:983–1055.
32. Hochstrasser D, Mertens F, Büttner H. Energy transport by lattice solitons in α-helical proteins. *Phys Rev A*. 1989;40(5):2602.
33. Jones C, Kopell N, Langer R. Construction of the FitzHugh-Nagumo pulse using differential forms. In: *Patterns and Dynamics in Reactive Media*. Springer; 1991:101–115.
34. Vainchtein A, Starosvetsky Y, Wright JD, Perline R. Solitary waves in diatomic chains. *Phys Rev E*. 2016;93:042210.
35. Lustri C, Porter MA. Nanoptera in a period-2 Toda chain. *SIAM J Appl Dyn Syst*. 2018;17(2):1182–1212.
36. Lustri CJ. Nanoptera and Stokes curves in the 2-periodic Fermi-Pasta-Ulam-Tsingou equation. *Physica D*. 2020;402:132239.
37. Toda M. *Theory of Nonlinear Lattices*. Springer-Verlag; 1989.
38. Chong C, Porter MA, Kevrekidis PG, Daraio C. Nonlinear coherent structures in granular crystals. *J Phys: Condens Matter*. 2017;29(41):413003.
39. Kevrekidis PG, Vainchtein A, Serra-Garcia M, Daraio C. Interaction of traveling waves with mass-with-mass defects within a hertzian chain. *Phys Rev E*. 2013;87:042911.
40. Kevrekidis PG, Stefanov AG, Xu H. Traveling waves for the mass in mass model of granular chains. *Lett Math Phys*. 2016;106(8):1067–1088.
41. Kim E, Li F, Chong C, Theocharis G, Yang J, Kevrekidis PG. Highly nonlinear wave propagation in elastic woodpile periodic structures. *Phys Rev Lett*. 2015;114(11):118002.

42. Vorotnikov K, Starosvetsky Y, Theocharis G, Kevrekidis PG. Wave propagation in a strongly nonlinear locally resonant granular crystal. *Physica D*. 2018;365:27–41.
43. Xu H, Kevrekidis PG, Stefanov A. Traveling waves and their tails in locally resonant granular systems. *J Phys A*. 2015;48(19):195204.
44. Faver TE, Goodman RH, Wright JD. Solitary waves in mass-in-mass lattices for antiresonance mass ratios. *Z Angew Math Phys*. 2020;71(6):197.
45. Faver TE. Small mass nanopteron traveling waves in mass-in-mass lattices with cubic FPUT potential. *J Dynam Differential Equations*. 2020.
46. Jayaprakash K, Vakakis AF, Starosvetsky Y. New family of solitary waves in granular dimer chains with no precompression. *Phys Rev E*. 2011;83:036606.
47. Jayaprakash K, Vakakis AF, Starosvetsky Y. Solitary waves in a general class of granular dimer chains. *J Appl Phys*. 2012;112(3):034908.
48. Jayaprakash K, Starosvetsky Y, Vakakis AF, Gendelman OV. Nonlinear resonances leading to strong pulse attenuation in granular dimer chains. *J Nonlinear Sci*. 2013;23:363–392.
49. Doedel EJ, Oldeman B. *Auto-07p: Continuation and Bifurcation Software*. Canada: Concordia Univ.; 1998.
50. Uecker H, Wetzel D, Rademacher JD. Pde2path – A Matlab package for continuation and bifurcation in 2D elliptic systems. *Numer Math: Theory Methods Appl*. 2012;7(1):58–106.
51. Chi H, Bell J, Hassard B. Numerical solution of a nonlinear advance-delay-differential equation from nerve conduction theory. *J Math Biol*. 1986;24:583–601.
52. Abell KA, Elmer CE, Humphries AR, Van Vleck ES. Computation of mixed type functional differential boundary value problems. *SIAM J Appl Dyn Syst*. 2005;4:755–781.
53. Elmer CE, Van Vleck ES. Computation of traveling waves for spatially discrete bistable reaction-diffusion equations. *Appl Numer Math*. 1996;20:157–169.
54. Elmer CE, Van Vleck ES. Analysis and computation of traveling wave solutions of bistable differential-difference equations. *Nonlinearity*. 1999;12:771–798.
55. Elmer CE, Van Vleck ES. Traveling wave solutions for bistable differential difference equations with periodic diffusion. *SIAM J Appl Math*. 2001;61:1648–1679.
56. Elmer CE, Van Vleck ES. A variant of Newton's method for the computation of traveling waves of bistable differential-difference equations. *J Dynam Differential Equations*. 2002;14:493–517.
57. Hupkes HJ, Verduyn-Lunel SM. Analysis of Newton's method to compute travelling waves in discrete media. *J Dynam Differential Equations*. 2005;17:523–572.
58. Crandall MG, Rabinowitz PH. Bifurcation from simple eigenvalues. *J Funct Anal*. 1971;8:321–340.
59. Zeidler E. *Applied Functional Analysis*. New York: Springer-Verlag; 1995:xvi+404. In: Applied Mathematical Sciences; vol. 109, Main principles and their applications.
60. Hoffman A, Wayne C. Counterpropagating two-soliton solutions in the Fermi-Pasta-Ulam lattice. *Nonlinearity*. 2008;21:2911–2947.
61. Lombardi E. *Oscillatory Integrals and Phenomena beyond All Algebraic Orders with Applications to Homoclinic Orbits in Reversible Systems*. Springer-Verlag Berlin Heidelberg; 2000. In: Lecture Notes in Mathematics; vol. 1741.
62. Johnson MA, Wright JD. Generalized solitary waves in the gravity-capillary Whitham equation. *Stud Appl Math*. 2020;144:102–130.
63. Hairer E, Lubich C, Wanner G. *Geometric Numerical Integration: Structure-Preserving Algorithms for Ordinary Differential Equations, Vol. 31*. Springer Science & Business Media; 2006.
64. Beyn W-J, Thümmler V. Freezing solutions of equivariant evolution equations. *SIAM J Appl Dyn Syst*. 2004;3(2):85–116.
65. Friesecke G, Mikikits-Leitner A. Cnoidal waves on Fermi-Pasta-Ulam Lattices. *J Dynam Differential Equations*. 2015;27(627–652).
66. Betti M, Pelinovsky DE. Periodic traveling waves in diatomic granular chains. *J Nonlinear Sci*. 2013;23(5):689–730.